

#### **OPEN ACCESS**

EDITED BY Wei Zhang, Guangzhou Marine Geological Survey, China

REVIEWED BY Min Luo, Shanghai Ocean University, China Junxi Feng, Guangzhou Marine Geological Survey, China

RECEIVED 08 July 2025
ACCEPTED 02 October 2025
PUBLISHED 22 October 2025

#### CITATION

Bai S, Xu H, Liu S, Dong L and Wu Z (2025) Organic carbon sources, transport, and mineralization in Kermadec Trench sediments.

Front. Mar. Sci. 12:1661587. doi: 10.3389/fmars.2025.1661587

#### COPYRIGHT

© 2025 Bai, Xu, Liu, Dong and Wu. This is an open-access article distributed under the terms of the Creative Commons Attribution License (CC BY). The use, distribution or reproduction in other forums is permitted, provided the original author(s) and the copyright owner(s) are credited and that the original publication in this journal is cited, in accordance with accepted academic practice. No use, distribution or reproduction is permitted which does not comply with these terms.

# Organic carbon sources, transport, and mineralization in Kermadec Trench sediments

Shuo Bai<sup>1</sup>, Hengchao Xu<sup>2</sup>, Shuangquan Liu<sup>2</sup>, Liang Dong<sup>3</sup> and Zijun Wu<sup>1\*</sup>

<sup>1</sup>State Key Laboratory of Marine Geology, Tongji University, Shanghai, China, <sup>2</sup>Institute of Deep-sea Science and Engineering, Chinese Academy of Sciences, Sanya, China, <sup>3</sup>School of Oceanography, Shanghai Jiao Tong University, Shanghai, China

Hadal trenches are critical hotspots for organic carbon (OC) deposition and diagenesis, yet the mechanisms controlling carbon sequestration, particularly the role of episodic tectonic and volcanic events, remain poorly constrained. This study integrates geochemical analyses of solid sediments and porewater from sediment cores collected at six stations along two transects in the Kermadec Trench to characterize OC sources, transport, and mineralization dynamics within this hadal trench system. Our results reveal a distinct south-to-north sediment transport pattern along the trench axis, leading to an accumulation of marine-derived OC in the south and terrestrial OC in the north. Importantly, earthquake-triggered turbidity currents in the central trench and volcanic eruptions in the north dominate episodic disturbances, exerting primary control over sediment deposition and diagenesis. These downslope currents transport significant OC fluxes from continental slopes to trench axes, enhancing burial rates 20-fold relative to steady-state sedimentation and promoting OC preservation in axial domains. Our findings demonstrate that spatial heterogeneity in hadal carbon cycling is primarily governed by episodic geological events, providing essential insights for accurate quantification of carbon fluxes and their integration into global biogeochemical models.

#### KEYWORDS

organic carbon mineralization, Kermadec Trench, event-driven deposition, carbon burial, volcanogenic sediments

### 1 Introduction

Marine sediments constitute a critical component of the global carbon cycle, serving as a major sink for marine and terrestrial organic carbon (OC) and a dynamic biogeochemical reactor regulating carbon diagenesis and burial (Krause-Jensen and Duarte, 2016; Steinberg and Landry, 2017; Arnosti et al., 2021). While OC reaching abyssal plains typically

undergoes extensive remineralization during descent, yielding predominantly refractory material with limited biogeochemical reactivity (Marsay et al., 2015; Cai and Jiao, 2023), hadal trenches-Earth's deepest marine environments exhibit distinct depositional dynamics. Their unique V-shaped topography, enclosed basins, and subduction-related compression create efficient sediment traps for particulate organic carbon (POC) (Leslie et al., 2017; Xie et al., 2024). Furthermore, gravitational downslope currents and recurring seismically triggered turbidity events (e.g., landslides, turbidity currents) actively transport OC from continental margins to trench axes (Linley et al., 2017; Tagliabue et al., 2017; Liu et al., 2023; Luo et al., 2025). This combination of passive accumulation and tectonically driven transport sustains localized zones of OC accumulation, challenging the long-standing paradigm of uniformly OCdepleted and biogeochemically inert hadal sediments (Peoples et al., 2018; Schauberger et al., 2021; Glud et al., 2013). Compounding this effect, the prevalence of hadal trenches in circum-Pacific regions with frequent volcanic activity introduces volcanic ash. Ash enhances deep-ocean carbon burial by acting as ballast to accelerate particle sinking and by releasing nutrients (particularly iron) that stimulate surface primary production, thereby amplifying OC export and improving burial efficiency (Watson, 1997; Adamo et al., 1993; Uroz et al., 2009; Hoffmann et al., 2012; Longman et al., 2019). Consequently, trenches constitute significant, previously underestimated hotspots for carbon processing in the marine carbon cycle.

Previous biogeochemical investigations in hadal zones have significantly advanced our understanding by examining spatial contrasts in carbon cycling between trench axes and adjacent slopes or abyssal plains (Luo et al., 2019; Li et al., 2020), highlighting differences in depositional regimes among global trench systems (Oguri et al., 2022; Xu et al., 2021), and characterizing lateral particle redistribution within trench environments (Glud et al., 2013). However, critical knowledge gaps persist regarding the spatial heterogeneity of carbon cycling within individual trenches. Significant uncertainties remain concerning variations along the trench axis (longitudinal), where carbon sources, transport pathways, and mineralization efficiency may differ even at comparable depths. Equally important is the need to quantify the interplay across the trench (cross-trench/transverse) between steady-state sedimentation and episodic tectonically driven sediment transport, governed by seismicity and trench geomorphology, and its impact on OC burial efficiency. To gain preliminary insights into these processes, carbon cycling within the Kermadec Trench (southwestern Pacific Ocean, north of New Zealand) was investigated. Analysis focused on six sediment cores collected along orthogonal bathymetric transects, combining sediment characterization (grain size, specific surface area, TOC,  $\delta^{13}$ C-TOC, XRD) with porewater geochemistry (DIC,  $\delta^{13}$ C-DIC,  $NO_3^-$ ,  $NH_4^+$ ,  $PO_4^{3-}$ ,  $SiO_3^{2-}$ ). This study aims to: (1) quantify the fractional contribution of different OC sources across distinct trench subdomains; (2) investigate relationships between depositional regimes (steady-state vs. event-driven) and OC mineralization; and (3) assess the effects of seismically triggered perturbations and volcanic material input on sedimentary OC burial.

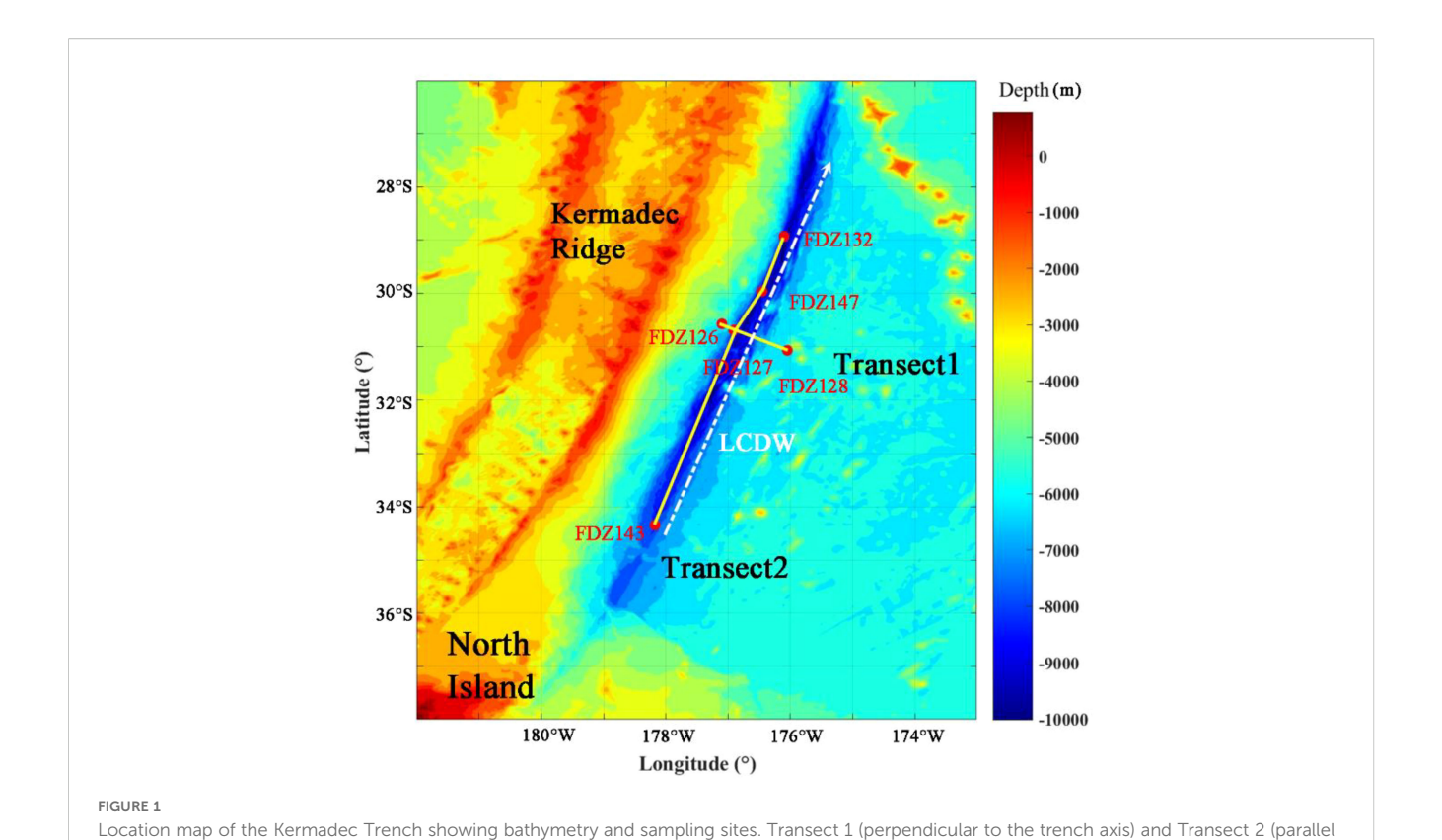
### 2 Materials and methods

## 2.1 Study area

The Kermadec Trench, a major hadal feature (>6,000 m depth) in the southwestern Pacific Ocean, extends approximately 1,200 km along a north-northeast axis with a maximum width of 120 km (Figure 1). This convergent margin results from the subduction of the Pacific Plate beneath the Australian Plate, generating complex seafloor geomorphology. Its southern terminus connects with the continental margin of New Zealand via the Hikurangi-Rapuhia transition zone, while its northern continuity with the Tonga Trench is disrupted by the Louisville Seamount Chain collision zone (Jamieson et al., 2020). The trench exhibits pronounced flank asymmetry, characterized by a steep Kermadec forearc slope along its western margin contrasting with the gentler gradient of the eastern Pacific Abyssal Plain (Lemenkova, 2019). A distinctive ~2,800-m-high basaltic escarpment on the northern ridge acts as a topographic barrier to Lower Circumpolar Deep Water, forcing northwestward flow to bifurcate and generating a trench-parallel current along the hadal axis (Germineaud et al., 2021). This tectonic-hydrodynamic coupling drives an efficient sediment routing system, with persistent axial currents advecting particulate material toward the trench floor. As a highly active seismic zone, the Kermadec Trench experiences frequent largemagnitude earthquakes that significantly alter sediment dynamics. Notable recent events include three M≥7 earthquakes on March 4, 2021, and 15 seismic events in 2022, culminating in a M7.9 earthquake in November 2022 (Peng et al., 2023; Ye et al., 2025). These earthquakes act as dominant geological drivers, triggering rapid morphological adjustments through mass wasting and generating cascading sedimentary disturbances.

### 2.2 Sample collection

During the China-New Zealand Joint Expedition (October–December 2022), six sediment push cores were retrieved from the Kermadec Trench using the manned submersible *Fendouzhe* and its support vessel *Tansuoyihao*. Sampling targeted six stations along bathymetric gradients (6,000–9,232 m water depth), encompassing three distinct geomorphological units: the continental slope (FDZ126), the abyssal plain (FDZ128), and four stations along the trench axis (FDZ127, FDZ132, FDZ143, FDZ147) (Table 1). Stations were strategically organized into two orthogonal transects (Figure 1): Transect 1 (W–E orientation, perpendicular to trench axis) spanning FDZ126 (slope)  $\rightarrow$  FDZ127 (axis)  $\rightarrow$  FDZ128 (plain), and Transect 2 (N–S orientation, parallel to trench axis) spanning FDZ132 (north axis)  $\rightarrow$  FDZ147 (central axis)  $\rightarrow$  FDZ127 (central axis)  $\rightarrow$  FDZ143 (south axis). Geospatial analysis confirmed the linear alignment of both transects, with inter-



to the trench axis) represent orthogonal sediment sampling profiles. The dashed white line indicates the flow path of Lower Circumpolar Deep

station distances calculated using the Haversine formula based on GPS coordinates. To facilitate subsequent location identification, station codes are appended with positional identifiers: FDZ126-LS (landward slope), FDZ127-MA (middle axis), FDZ128-AP (abyssal plain), FDZ132-NA (north axis), FDZ147-NA (north axis), and FDZ143-SA (south axis).

Water (LCDW).

Upon retrieval, sediment cores were immediately transferred to the onboard laboratory for dissolved oxygen (DO) measurements

TABLE 1 Sampling site locations, coordinates, and depths in the Kermadec Trench.

| Core<br>id | Water<br>depth (m) | Latitude<br>(°S) | Longitude<br>(°W) | Position               |
|------------|--------------------|------------------|-------------------|------------------------|
| FDZ126     | 6000               | 30.57129         | 177.0993          | Landward<br>slope (LS) |
| FDZ127     | 7600               | 30.68897         | 176.9093          | Middle axis<br>(MA)    |
| FDZ128     | 5825               | 31.0691          | 176.0487          | Abyssal plain<br>(AP)  |
| FDZ132     | 8922               | 28.92912         | 176.1016          | North axis<br>(NA)     |
| FDZ147     | 9232               | 29.96038         | 176.4529          | North axis<br>(NA)     |
| FDZ143     | 7422               | 34.34497         | 178.1729          | South axis (SA)        |

and subsequent porewater extraction. Pre-drilled access holes at 2 cm vertical intervals, sealed with tape prior to deployment to preserve core integrity, maintain core integrity, facilitated both processes. Although autonomous benthic landers provide the highest accuracy for porewater DO measurements by minimizing artifacts associated with core retrieval (e.g., pressure changes, temperature shifts, and oxygen consumption during ascent) (Glud, 2008), our shipboard protocol prioritized rapid processing to minimize atmospheric exposure. DO measurements were performed first using a calibrated Unisensor (Denmark) microelectrode. Following immediate removal of the tape seal, the electrode was inserted through the access holes, and measurements were recorded upon signal stabilization. This approach provided a preliminary characterization of the oxygen gradient within the inherent constraints of *ex situ* shipboard analysis.

Porewater was subsequently extracted using Rhizon soil moisture samplers (5 cm length, 0.1  $\mu$ m pore size inert polymer tubes). Vacuum pressure applied via disposable 20 mL syringes, yielding approximately 15 mL of porewater per 2 cm interval over a 3-hour extraction period. Extracted porewater were immediately processed for preservation. Aliquots for nutrient analysis were stored in centrifuge tubes at -20 °C. Subsamples for dissolved inorganic carbon (DIC) analysis were preserved in 2 mL glass vials with 10  $\mu$ L of saturated HgCl<sub>2</sub> solution, sealed, and stored at 4 °C to inhibit microbial activity. Although HgCl<sub>2</sub> preservation may affect DIC measurements in porewater with high H<sub>2</sub>S concentration (Argentino et al., 2023), its impact is negligible here due to the

shallow (<30 cm) sediment depth of our hadal samples, which typically exhibit very low H<sub>2</sub>S levels. After porewater collection, sediment cores were sectioned at 2 cm intervals and stored at -20 °C for subsequent solid geochemical analysis.

### 2.3 Analytical methods

### 2.3.1 Solid sediment analysis

Sediment grain size analysis was conducted using a Malvern Mastersizer 2000 laser particle size analyzer (Malvern Instruments Ltd., UK) at the State Key Laboratory of Marine Geology, China. Freeze-dried samples were homogenized by grinding with a mortar. Aliquots (2–5 g) were dispersed in 0.5% (w/v) sodium hexametaphosphate (NaPO<sub>3</sub>)<sub>6</sub> for 24 hours before analysis. Analytical precision, determined from replicate sample analysis (n = 6), was within ±3%. Specific surface area (SSA) was determined via a 5-point BET nitrogen adsorption isotherm according to Yao et al. (2014). Approximately 1 g of freeze-dried sediment was decarbonated at 350 °C for 12 hours to remove organic matter (OM), degassed at 200 °C for 30 minutes, and subsequently analyzed under liquid nitrogen conditions.

For elemental and stable carbon isotope analysis, following the method of Luo et al. (2019), freeze-dried sediment samples were homogenized using an agate mortar and pestle. Aliquots (2-3 g) were weighed (pre-acidification weight) and treated with 1 M HCl at room temperature to remove inorganic carbon. After centrifugation (3,500 × g, 10 min), supernatants were decanted, and residues were rinsed thrice with ultrapure water. The decarbonated sediments were then re-freeze-dried, re-weighed (post-acidification weight), and rehomogenized prior to analysis. Total organic carbon (TOC) and total nitrogen (TN) measurements were calibrated using the mass difference (weight loss) between preand post-acidification weights, which accounts for inorganic carbon removal. TOC and TN contents, along with  $\delta^{13}$ C values of organic carbon (δ13C-TOC), were determined using a Vario EL cube elemental analyzer (Elementar, Germany) coupled via continuous flow to an IsoPrime 100 isotope ratio mass spectrometer. The  $\delta^{13}$ C values are reported in per mil (%) relative to the Vienna Pee Dee Belemnite standard (V-PDB). Measurement precision, assessed through replicate analyses, yielded average standard deviations of  $\pm 0.03\%$  for TOC,  $\pm 0.007\%$  for TN, and  $\pm 0.2\%$  for  $\delta^{13}$ C.

Sediment mineralogy was analyzed using an X-ray diffractometer (PANalytical X'Pert Pro) with Cu Kα radiation at 40 kV and 40 mA. Scans were conducted over 4–80° 2θ with a 0.033° step size and 0.5 s counting time per step. Phase identification was performed using Profex software by matching peaks to ICDD database standards. Semi-quantitative abundance was determined via Rietveld refinement. Triplicate analyses yielded <5% RSD for major phases (>10 wt%).

### 2.3.2 Porewater analysis

Porewater DIC concentrations and carbon isotopic composition ( $\delta^{13}$ C-DIC) were measured using a Gas Bench II peripheral device (Thermo Fisher Scientific) coupled to a Delta V Advantage isotope

ratio mass spectrometer (IRMS). Samples were acidified with 100  $\mu L$  phosphoric acid (H<sub>3</sub>PO<sub>4</sub>, 99%) in 12 mL helium-flushed Exetainer vials, followed by 2-hour equilibration at 25 °C. The system was calibrated daily with NaHCO<sub>3</sub> standards (0.5–10 mM) and certified reference material IAEA-C3. Measurement accuracy (± 2%) was validated through spike recovery tests, with analytical precision controlled to <0.15% based on replicate analyses. Isotopic values are reported in  $\delta$ -notation relative to the Vienna PeeDee Belemnite (VPDB) standard.

Nutrient concentrations ( $\mathrm{NO_3}^-$ ,  $\mathrm{NH_4}^+$ ,  $\mathrm{PO_4}^{3-}$ ,  $\mathrm{SiO_3}^{2-}$ ) were determined using a QuAAtro continuous flow analyzer (Seal Analytical) equipped with 550 nm/880 nm dual detectors and employing standard photometric methods. Daily calibration curves ( $\mathrm{R}^2 > 0.999$ ) were established using mixed standard solutions. Analytical precision was monitored through triplicate analyses of every 10th sample, with relative standard deviations < 3%. Dissolved iron concentrations were determined using ICP-AES (IRIS Advantage). Prior to analysis, samples were diluted 1:30 (v/v) and spiked with scandium internal standard (0.5 mg/L), with measurement precision better than 5%.

### 2.3.3 Data analysis and statistics

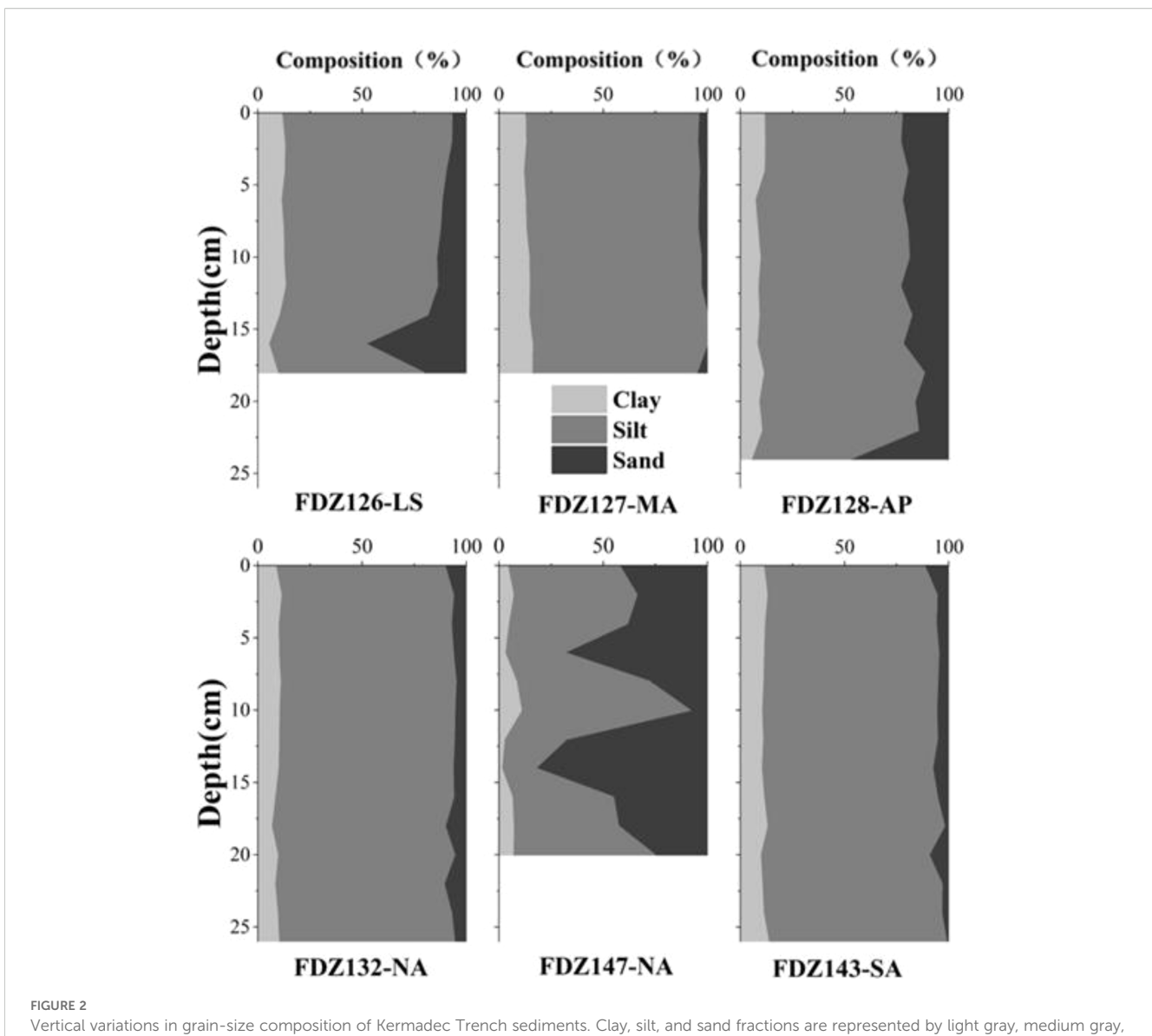
To determine the relative contributions of different OC sources in the Kermadec Trench, a three-end-member mixing model was employed using  $\delta^{13}$ C values and the C/N ratios of bulk OC. This model quantified the fractional contributions of three distinct sources to the total OC pool: (1) marine phytoplankton-derived OC (OC<sub>mar-fresh</sub>); (2) terrestrial OC (OC<sub>terr-fresh</sub>); and (3) microbereworked OC (OC<sub>reworked</sub>), which comprises highly altered allochthonous OC (both marine and terrestrial) along with in situ living and dead microbes. The marine end-member (OC<sub>mar-fresh</sub>) was assigned characteristic values for Southern Ocean phytoplankton:  $\delta^{13}C = -21.2\%$  and C/N = 6 (Popp et al., 1999). The terrestrial end-member (OCterr-fresh) was assigned values representative of New Zealand rivers:  $\delta^{13}C = -26.5\%$  and C/N = 12 (Leithold et al., 2006). For the microbe-reworked end-member  $(OC_{reworked})$ , characteristic values of  $\delta^{13}C = -20.0\%$  and C/N = 3.7were assigned, based on data from trenches of similar depth (Li et al., 2020).

To quantify uncertainties in calculated OC fractions arising from end-member value variability, a Bayesian Markov chain Monte Carlo (MCMC) simulation with random sampling was implemented in MATLAB R2021b (MathWorks Corporation, USA). This approach, following Anderson (2011), propagated end-member uncertainty to assess its impact on source contribution estimates.

## 3 Results

## 3.1 Sediment geochemical characteristics

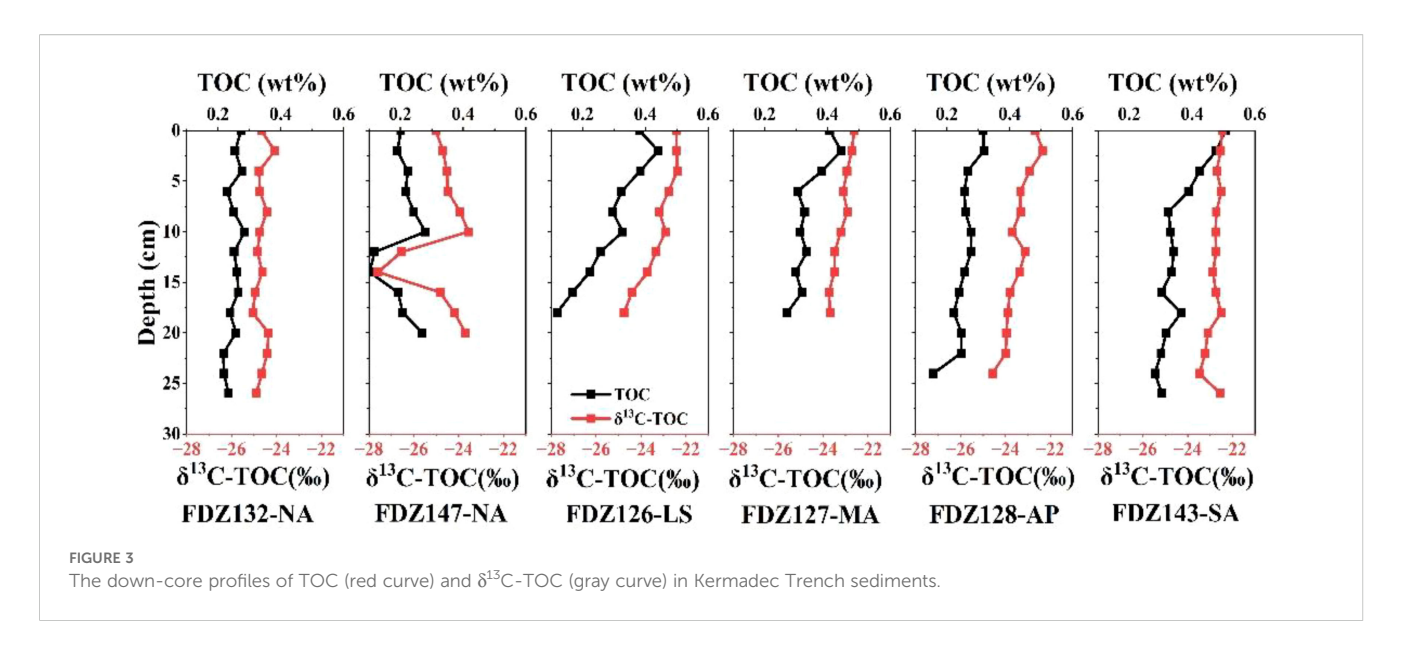
Sediments within the Kermadec Trench are predominantly silty (77.2–86.4% silt), with minor clay (6.4–15.8%) and sand (0–10.3%) fractions (Figure 2). Median grain size ( $D_{50}$ ) ranges from 6.7 to 11.1



Vertical variations in grain-size composition of Kermadec Trench sediments. Clay, silt, and sand fractions are represented by light gray, medium gray and black shading, respectively.

 $\mu m$  (mean  $\pm 1\sigma$ : 8.9  $\pm$  1.4  $\mu m$ ). Station FDZ147-NA exhibits anomalous granulometry, characterized by highly variable sand content (8.4-82.5%) and a maximum  $D_{50}$  of 69.8  $\mu$ m, accompanied by reduced silt-clay fractions (17.5-91.6%). Our preliminary comparison of adjacent sedimentary settings reveals distinct regimes: the abyssal plain sediments contain 11.7-47.2% sand (D<sub>50</sub>: 12.03  $\pm$  2.1  $\mu$ m), slightly coarser than those on the landward slope (0–48.5% sand;  $D_{50}$ : 11.21  $\pm$  3.4  $\mu$ m). Two obvious sand-rich layers were identified: one containing 48.5% sand at 16 cm depth in FDZ126-LS ( $D_{50}$  = 15.8  $\mu m$ ), and the other with 47.2% sand at 24 cm depth in FDZ128-AP ( $D_{50}$  = 14.3  $\mu m$ ). These horizons exhibit >300% sand enrichment relative to adjacent strata, suggesting episodic high-energy deposition. The SSA values display significant spatial heterogeneity (12.49-84.95 m<sup>2</sup>/g; Supplementary Table S1). Northern trench axis stations exhibit systematically higher SSA than southern counterparts, peaking at 84.95 m<sup>2</sup>/g (FDZ147-NA). Cross-trench transects reveal a consistent SSA pattern: abyssal plain > trench axis > landward slope.

TOC decreases from 0.51% (surface, FDZ143-SA) to 0.16% (24 cm, FDZ128-AP), while TN declines from 0.08% to 0.02% (Figure 3). Notably, FDZ147-NA exhibits coupled extremes: minimum TOC (0.10% at 14 cm) coincides with maximum SSA (84.95 m²/g) and sand content (82.5%), suggesting grain-size mediated organic matter preservation. Along the trench axis, TOC decreases latitudinally from 0.43  $\pm$  0.08% (south) to 0.21  $\pm$  0.05% (north), coinciding with increasing water depth (9,240 m at FDZ143-SA to 10,050 m at FDZ147-NA). Perpendicular to the axis, surface sediment TOC shows distinct zonation: landward slope deposits contain 31% more TOC than trench axis sediments, which exceeds abyssal plain values by 21%. The steepest gradient occurs between landward slope and trench axis ( $\Delta$ TOC = 0.09%/km), compared to 0.05%/km from trench axis to abyssal plain.

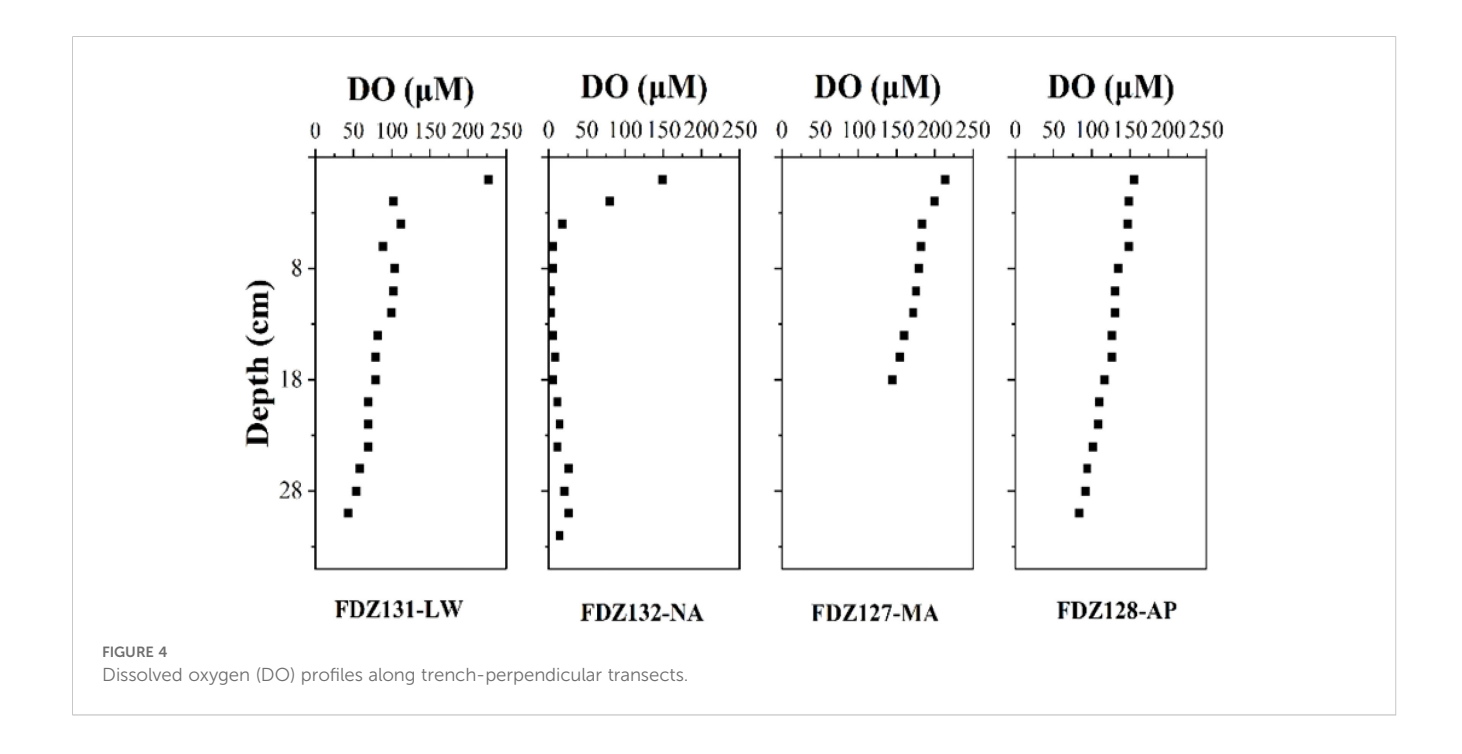


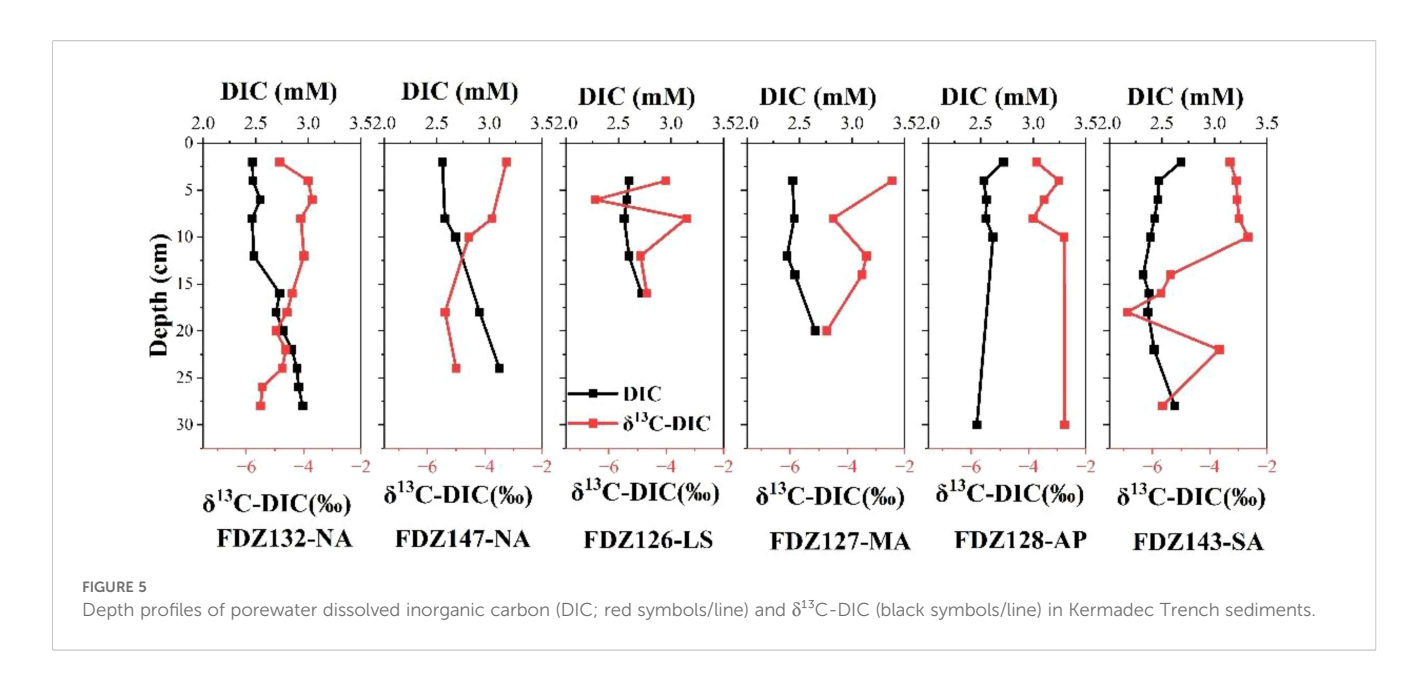
XRD analysis of selected layers (based on grain size distribution and porewater geochemistry; Supplementary Figures S1, S2, Supplementary Table S2) reveals hadal sediments are dominated by muscovite (avg. 28%), albite (avg. 34%), quartz (avg. 19%), and chlorite (avg. 11%), with albite as the primary phase. Volcanic material (clinoferrosilite and enstatite) was identified at FDZ147-NA (northern trench; 2 cm and 20 cm depths) and FDZ128-AP (abyssal plain; 24 cm depth). These volcanic-rich horizons correlate strongly (R² = 0.59) with sand content. Clinoferrosilite content peaked at 17.7% (20 cm layer, FDZ147-NA) but remained below 8% at FDZ132-NA. No volcanic ash was detected at FDZ126-LS or FDZ143-SA; however, the sand-rich layer at 16 cm depth in FDZ126-LS corresponded to elevated albite (40%), while FDZ127-MA contained trace ferrosilite (1%). Kaolinite was consistently

detected at four axial trench stations (avg. 13.88%; Supplementary Figures S1 S2, Supplementary Table S2).

### 3.2 Porewater geochemical distribution

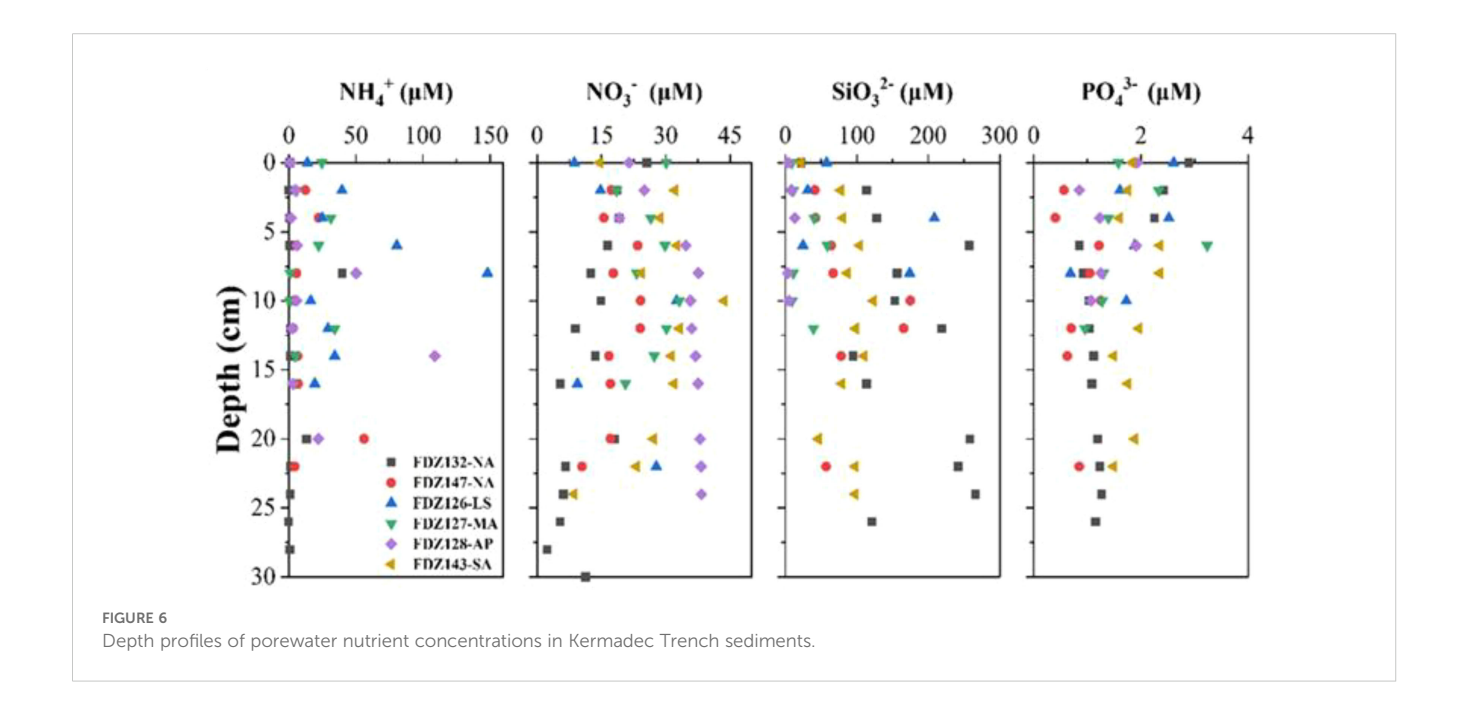
Cross-trench porewater DO profiles reveal redox zonation correlated with geomorphological position (Figure 4). Station FDZ131, located on the continental slope adjacent to FDZ132-NA (Supplementary Figure S3), exhibits complete oxygen depletion below 5 cm depth (DO  $< 4~\mu mol/L)$ . Stations along Transect 1 (FDZ127-MA–FDZ128-AP) show a transitional redox regime, maintaining oxic conditions down to 20 cm depth. Porewater DIC concentrations generally increase with sediment depth,





ranging from 2.48  $\pm$  0.15 mM at 0–15 cm to 3.82  $\pm$  0.23 mM at 30–40 cm (Figure 5). However, DIC concentrations lack a clear spatial distribution pattern. Notably, DIC- $\delta^{13}$ C values revealed anomalies: at the southernmost station FDZ143-SA, values were enriched within 0–10 cm but sharply depleted below 12 cm. All three Transect 1 stations exhibit a DIC- $\delta^{13}$ C inflection point at 6–8 cm depth, potentially indicating intensified mineralization within this layer. Porewater NO<sub>3</sub><sup>-</sup> and NH<sub>4</sub><sup>+</sup> distributions show pronounced spatial heterogeneity (Figure 6). Both landward slope and abyssal plain environments exhibit peak NH<sub>4</sub><sup>+</sup> accumulation (>100  $\mu$ M below 5 cm depth). In contrast, trench-axis stations maintain low NH<sub>4</sub><sup>+</sup> concentrations (<10  $\mu$ M below 2 cm), with only FDZ127-MA showing surface enrichment (49.3  $\mu$ M). Nitrate (NO<sub>3</sub><sup>-</sup>)

concentration correlates with oxygen availability. At the anoxic site FDZ132-NA, NO $_3^-$  decreases with depth from 25.5  $\mu$ M at the surface. Conversely, at the oxic Transect 1 stations, NO $_3^-$  increases with depth, following the order FDZ128-AP > FDZ127-MA > FDZ126-LS. Phosphate (PO $_4^{3-}$ ) concentrations show a slight north-to-south increasing trend, while silicate (SiO $_3^{2-}$ ) concentrations exhibit a southward decrease (Figure 6). Dissolved iron (Fe) concentrations were generally low across the study area, with detectable levels found in only six sediment layers. Three layers in core FDZ147-NA showed Fe concentrations increasing with depth, reaching a maximum of 3.1 mg/L (Supplementary Table S3). Detectable Fe was also present in single layers at sites FDZ126-LS, FDZ127-MA, and FDZ143-SA.



### 4 Discussion

# 4.1 Sources and transport of organic carbon in the Kermadec Trench

To investigate spatial variations in OC and its transport within Kermadec Trench sediments, we grouped sampling stations into two transects based on distinct geomorphological settings. Transect 1 traverses the landward slope, trench axis, and abyssal plain, capturing a cross-sectional profile. Transect 2 follows the central trench axis along a north-south orientation, representing its longitudinal axis. This strategic grouping captures contrasting sedimentary depositional regimes, enabling comparative analysis of OC sources and transport pathways between the cross-section of trench and longitudinal axis. The transect-based approach thus facilitates systematic evaluation of how topographic position and sediment transport dynamics influence OC distribution patterns in these hadal environments.

# 4.1.1 The landward slope-trench axis-abyssal plain transect (transect 1)

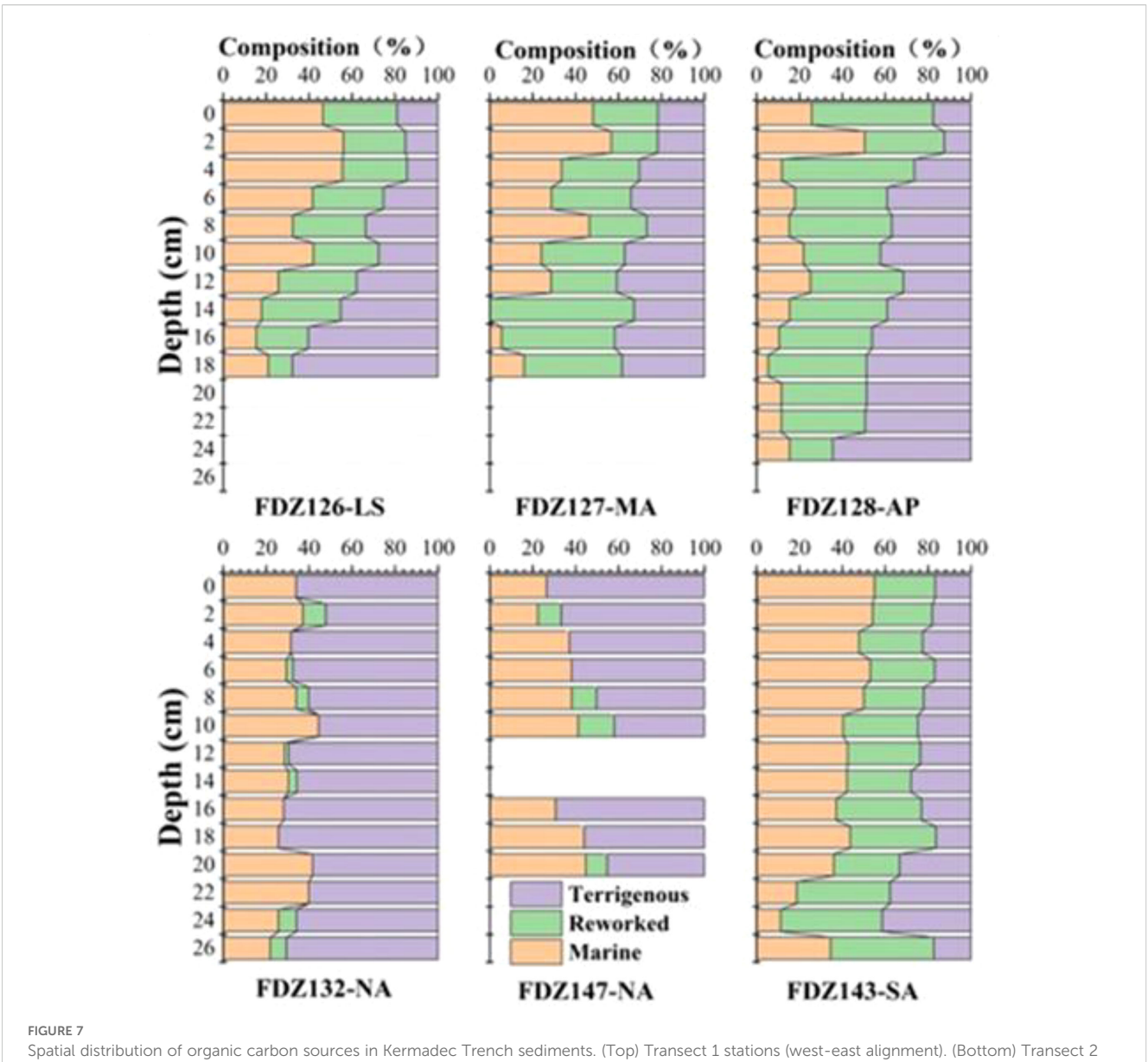
Organic carbon (OC) accumulation in hadal trenches is governed by multiple factors. The unique topography of these systems, characterized by steep slopes converging towards the trench axis, significantly enhances sediment focusing and promotes OC accumulation within the axis, as demonstrated in prior studies (Wenzhöfer et al., 2016; Li et al., 2020; Xu et al., 2021). Within trench sedimentary systems-comprising landward slopes, the trench axis, and adjacent abyssal plains, the primary sources of sedimentary OC are typically marine-sourced OC derived from surface water primary productivity and terrigenous OC originating from adjacent landmasses (Kermadec Ridge and north island of New Zealand) (Xu et al., 2021). Crucially, microbially reworked OC represents a distinct and significant third end-member, contributing substantially to the sedimentary OC pool (Fang et al., 2000; Jiao, 2012; Li et al., 2020). Evidence from the Yap Trench, where microbially reworked OC can constitute up to 90% of sedimentary OC in specific layers, underscores its potential dominance and transformative role in OC preservation (Li et al., 2020). Using  $\delta^{13}$ C-TOC and C/N as tracers, we found that surface sediments along Transect 1 are dominated by marine-sourced and microbially reworked OC, collectively accounting for 80% of OC, with terrigenous OC contributing only 20% (Figure 7). This indicates consistent OC sources across profiles perpendicular to the trench axis. Porewater oxygen concentrations further support this similarity, exhibiting comparable trends perpendicular to the axis (Figure 4). Fine-grained sediments typically exhibit high SSA, whereas coarse-grained sediments show the opposite trend (Mayer, 1994). This relationship is evident in our data: Station FDZ127-MA (average sand content: 3.6%; SSA: 28.44 m²/g) displays higher SSA than FDZ126-LS (average sand content: 16.4%; SSA: 17.81 m<sup>2</sup>/g) (Figure 8). Similarly, the maximum grain size at 16 cm depth in core FDZ126-LS corresponds to the minimum SSA. However, an anomaly occurs at station FDZ128-AP, which exhibits high sand content (average: 21.48%) yet elevated SSA (average: 30.27 m²/g)

compared to trench axis and landward slope stations (Supplementary Table S1). XRD analysis reveals that the mineral composition in the sandy layer at depth is similar between FDZ126-LS and FDZ127-MA, though FDZ126-LS contains higher quartz and muscovite content. In contrast, the sandy layer at FDZ128-AP contains 11.93% ferrosilite (Supplementary Figure S2, Supplementary Table S2), suggesting distinct sedimentary events in the continental slope and abyssal plain. Grain size variations at FDZ126-LS indicate turbidity current sedimentation, potentially earthquake-triggered, whereas the sand peak at FDZ128-AP likely reflects volcanic ash input (detailed discussion in Section 4.3). No analogous basal peak occurs at the trench axis station, likely because the funnel-shaped topography concentrates sediments, and weak hydrodynamics coupled with high sedimentation rates bury coarsegrained material deeper than sampled. In undisturbed surface sediments along Transect 1, sand content decreases in the order: abyssal plain > continental slope > trench axis. This trend contrasts with findings from the Yap Trench (Li et al., 2020), potentially due to the gentler continental slope of the Kermadec Trench, which diminishes sediment transport from the Kermadec Ridge to the trench axis (Lemenkova, 2019).

### 4.1.2 The trench-axis transect (transect 2)

The trench axis, representing the deepest region, exhibits significant sedimentary heterogeneity (Stewart and Jamieson, 2018). Material supply to trench axis varies considerably, evidenced by differences in benthic faunal size (Du et al., 2021), surface ocean primary productivity, and sedimentary OC content (Behrenfeld and Falkowski, 1997; Peoples et al., 2019). This heterogeneity is reflected locally in the abnormally high silt and ferrosilite contents at station FDZ147-NA (Supplementary Figure S2, Supplementary Table S2), potentially attributable to the January 5, 2022, volcanic eruption near Nuku'alofa, Tonga, north of the Kermadec Trench. Beyond local differences, sediments along the Kermadec Trench axis exhibit a distinct north-south gradient. The northern segment is characterized by basaltic andesite, contrasting with turbidites of New Zealand origin dominating the south (George et al., 2005). Consistent with this lithology, augite contents are higher at northern stations (FDZ132-NA, FDZ147-NA) than at southern stations (FDZ127-MA, FDZ143-SA), suggesting north-to-south transport of volcanic materials.

The ratio of total organic carbon to specific surface area (TOC/SSA), termed OC loading, quantifies the mass of OC associated with a unit area of mineral surface (Blair and Aller, 2012). This parameter serves as a critical indicator for differentiating the sources and supply mechanisms of OC across diverse sedimentary environments. In this study, the TOC and OC loading along the axis show a gradual decrease from south to north. Along this gradient, the contribution of terrigenous OC increases, while marine-derived and microbially reworked OC decreases (Figure 7). Marine and microbially reworked OC dominate (80%) at central and southern stations, contrasting sharply with the north where marine-sourced OC constitutes only ~30% and microbially reworked OC is minimal. These data reveal a distinct south-to-north spatial gradient in sedimentary



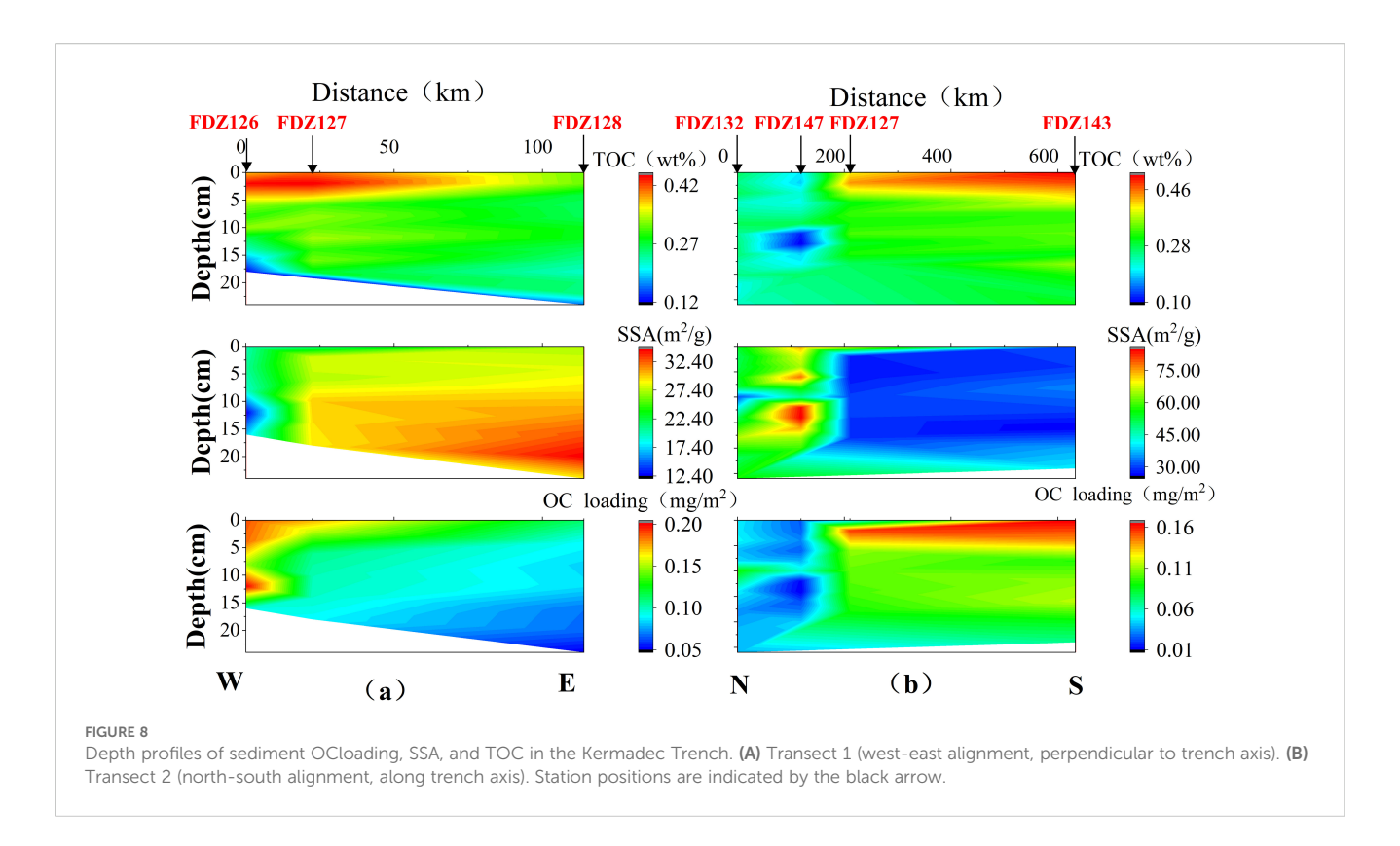
stations (north-south alignment).

organic matter composition. This gradient aligns with the flow direction of the Lower Circumpolar Deep Water (south-to-north along the axis), suggesting current-controlled material transport along the Kermadec Trench axis.

# 4.2 Mineralization of organic matter in the Kermadec Trench

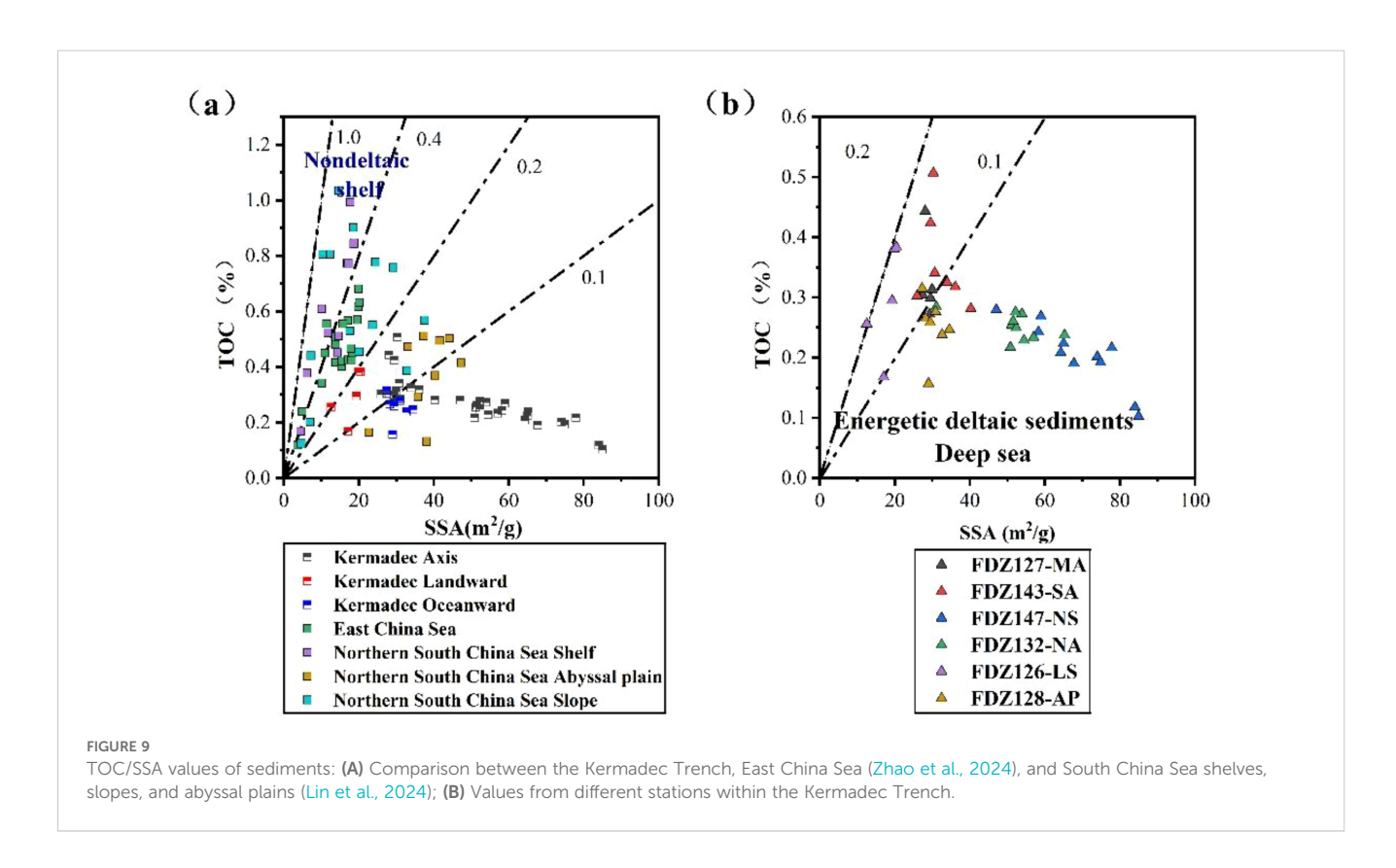
The extreme pressure characteristic of trench environments may promote the breakdown of recalcitrant organic materials (Luo et al., 2018). Theoretically, sedimentary organic matter mineralization is fundamentally governed by Gibbs free energy, dictating the sequence of electron acceptor utilization (e.g., O<sub>2</sub>,

NO<sub>3</sub><sup>-</sup>, Mn(IV), Fe(III), SO<sub>4</sub><sup>2-</sup>) (Arndt et al., 2013). Measurements in the Kermadec Trench reveal localized oxygen penetration depths exceeding 20 cm (Figure 4; Xiao et al., 2024), coupled with generally higher oxygen consumption rates at the trench axis compared to adjacent regions (Glud et al., 2013). These observations confirm that aerobic respiration dominates OC mineralization in these sediments. Consistent porewater oxygen profiles across the continental slope-trench axis-abyssal plain transect (perpendicular to the trench axis) further support this primary aerobic pathway. Beyond aerobic respiration, key hypoxic processes contribute to OC cycling: denitrification consumes NO<sub>3</sub><sup>-</sup> and organic matter to produce N<sub>2</sub>, while ammonification during early diagenesis generates NH<sub>4</sub><sup>+</sup> (Cai et al., 2010; Chen et al., 2023). Nitrification, evidenced by



relatively high  $\mathrm{NO_3}^-$  content in Transect 1, which is also significant in trench surface sediments. Elevated  $\mathrm{PO_4}^{3-}$  and  $\mathrm{SiO_3}^{2-}$  concentrations throughout the system provide additional evidence for active mineralization.

The TOC/SSA ratio reflects sediment exposure time and the influence of sedimentary processes on OC accumulation (Mayer, 1994; Li et al., 2017, 2020). TOC/SSA values < 0.4 typically indicate prolonged oxygen exposure, reducing sediment mineralization



capacity (Blair and Aller, 2012). Data comparisons with the East China Sea and South China Sea (Figure 9a) show that OC loading values (0.1–0.2) in parts of the South China Sea shelf and abyssal plain influenced by riverine suspended sediments indicate moderate mineralization potential. Surface sediments at stations FDZ126-LS, FDZ127-MA, and FDZ143-SA (proximal to land) fall within this range, suggesting retained mineralization potential. In contrast, TOC/SSA values < 0.1 at stations FDZ132-NA and FDZ147-NA (northern study area) are comparable to that in some areas of the abyssal plain of the South China Sea, indicating limited mineralization potential (Figure 9b).

As previously noted, station FDZ147-NA is influenced by volcanic ash input. The overall increase in TOC content with depth suggests volcanic ash facilitates TOC preservation. However, a distinct TOC minimum observed at the 14-16 cm depth interval likely results from dilution by a concentrated layer of volcanic ash accumulation at this horizon. Furthermore, porewater nitrate concentrations at FDZ147-NA are relatively low compared to central and southern stations (FDZ126-LS, FDZ127-MA, FDZ128-AP, FDZ143-SA). This observation aligns with the previously described pattern of suppressed mineralization. Additionally, enriched silicate concentrations in the porewater of the ash-rich sediment layer suggest active dissolution and release of silica from the volcanic material. Collectively, the observed low NO<sub>3</sub><sup>-</sup> concentrations, coupled with elevated porewater silicate levels indicative of active ash dissolution, point to a dual role for volcanic input: it acts as a source of reactive silica while simultaneously enhancing OC preservation. This enhancement likely arises from the formation of stabilizing mineral-organic associations (Zhao et al., 2024; Huang et al., 2023). Consequently, mineralization processes in trench surface sediments are controlled not only by water depth but also significantly by volcaniclastic input, with episodic ash deposition exerting a primary influence on OC mineralization and preservation.

## 4.3 Sedimentary processes in the Kermadec Trench: influence of earthquakes and volcanogenic input

Earthquake-triggered disturbances significantly enhance sediment transport from landward slopes into trenches via lateral transport (Kioka et al., 2019). The V-shaped trench morphology, combined with earthquake-induced turbidity currents, facilitates efficient particulate matter transport along the trench axis (Talling et al., 2024; Turnewitsch et al., 2014). Such events typically deposit sediment layers 30 cm to 1 m thick within trenches. For instance, the 2011 Tohoku earthquake deposited a 31 cm-thick sandy layer on the Japan Trench seafloor within a short period (Oguri et al., 2013). Similarly, sediments exhibiting positive grading and anomalously high sand content were observed at depths of 5–16 cm in Transect 1 of this study, suggesting deposition by earthquake-triggered turbidity currents. Given frequent seismic activity of the Kermadec Trench, including a magnitude 6.6 shallow-focus earthquake (intensity VI) west of the FDZ126-LS observatory on

August 14, 2022 (USGS), we speculate that this event caused the anomalously high sand content via turbidity current deposition.

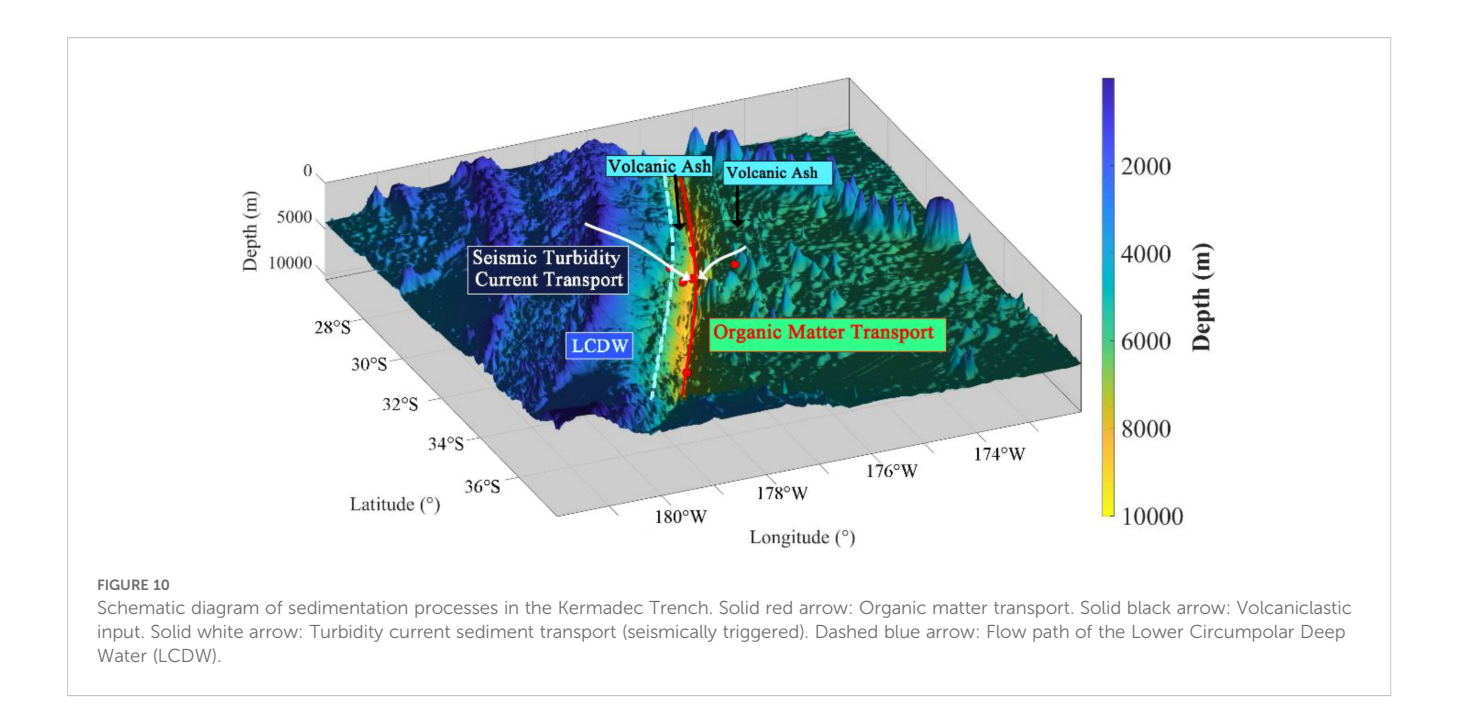
Earthquake-generated turbidity currents enable rapid OC deposition. The OC deposition rate is quantified as:

$$OC$$
 deposition rate =  $LSR \times TOC \times DBD$ 

where OC deposition rate is in g m<sup>-2</sup> yr<sup>-1</sup>, LSR is the linear sedimentation rate (cm yr<sup>-1</sup>), TOC is the total OC content (wt%, g OC  $g^{-1}$  dry sediment), and DBD is the dry bulk density (g cm<sup>-3</sup>).

Previous studies on the Kermadec Trench have shown that under stable conditions, the linear sedimentation rate (LSR) measured on the southern side of FDZ126-LS is  $2.01 \times 10^{-2}$  cm yr<sup>-1</sup>, and the average dry bulk density (DBD) is 1.49 g cm<sup>-3</sup> (Xu et al., 2021). Based on grain size distribution profile, the sediment thickness deposited during the interval from the earthquake occurrence to sampling (three months) was set at 16 cm. The TOC content in the bottom layer of FDZ126-LS is 0.22 wt%, which was used to estimate the OC buried in this single event. Calculations based on the above data indicate that the amount of event-driven OC transport and preservation is at least 20-fold higher than that under stable sedimentation conditions. High-frequency seismicity in subduction trenches drives sedimentary OC burial via earthquake-triggered turbidity currents and mass wasting. These events likely dominate OC sequestration in hadal systems, potentially constituting a major pathway in global carbon budgets. In contrast to its influence on sediment burial efficiency, seismic activity also exerts a strong control on porewater oxygen dynamics and sediment mineralization. Oxygen penetration depth (OPD) exceeds 20 cm at stations FDZ127-MA and FDZ128-AP, contrasting sharply with only 10 cm at FDZ132-NA, which experiences minor seismic influence. This disparity is attributed to seismically triggered turbidity currents in Transect 1, enhancing sediment oxygenation (Fernandes et al., 2016). The resulting increased OPD intensifies surface OC mineralization, evidenced by elevated NO<sub>3</sub><sup>-</sup> and PO<sub>4</sub><sup>3-</sup> concentrations (0-8 cm depth) across all Transect 1 stations (Figure 6).

Beyond seismic activity, volcanic eruptions represent another major geological force shaping sediment composition and biogeochemical cycling in the Kermadec Trench system. The January 5, 2022, eruption north of the trench (Tonga) significantly reshaped these processes. XRD analysis reveals a north-to-south decrease in volcanic ash content within trench sediments (Supplementary Table S2), indicating dominant ash transport in this direction. This volcanic input correlates with sediment properties: higher SSA corresponds to OC loading (Figure 8), with XRD confirming abundant volcanic ash in these high-SSA layers (Supplementary Figures S1-2, Supplementary Table S2). Sediment provenance varies spatially: at FDZ126-LS, a sand content peak at 10-15 cm depth coincides with minimum SSA, indicating turbidity current-transported material. In contrast, FDZ128-AP and FDZ147-NA sediments are predominantly volcaniclastic. This pattern suggests seismic disturbances facilitate transport of slope-derived OC into the trench interior, while rapid volcanic deposition dilutes OC on the abyssal plain at our site. Supporting this, TOC content increases with depth at FDZ147-NA.



Critically, the absence of positive grading at FDZ147-NA confirms its volcanogenic sand provenance, independent of seismic activity, consistent with the 2022 eruption's influence north of the trench. Although volcanic ash generally facilitates organic matter preservation, concurrent mineralization occurs during burial. This eruptive event further modulated mineralization processes, evidenced by a strong negative correlation ( $R^2 = 0.975$ , p < 0.01) between dissolved Fe and  $\delta^{13}$ C-DIC in porewater (Supplementary Figure S4). Heterotrophic Fe(II)-oxidizing bacteria utilize structural iron within igneous minerals, releasing bioavailable Fe and associated metallic elements. Strains isolated from volcanic ash exhibit heterotrophic Fe(II) oxidation coupled with nitrate reduction (Sudek et al., 2017), providing a plausible mechanism for the observed denitrification at 5-10 cm depth along Transect 1. Integrating these findings with the established depositional pattern (landward slope → trench axis → abyssal plain), we infer that material derived from the southern slope is transported northward along the trench axis by ocean currents, influenced by the New Zealand North Island. During transport, marine OC undergoes gradual mineralization, whereas terrestrial OC accumulates in the northern trench. Meanwhile, earthquake-triggered turbidity currents on the landward slope facilitate rapid burial of OC. Given the eruption's location north of the trench, the northern trench axis receives substantial volcaniclastic input. In contrast, the abyssal plain is influenced by both volcaniclastic density currents and deposition of surface-derived marine plankton, as illustrated in Figure 10.

### 5 Conclusions

Geochemical analyses of sediments and porewater from the Kermadec Trench reveal a complex interplay between sediment

sources, depositional processes, and mineralization dynamics. Sediments exhibit a distinct south-to-north transport trajectory along the trench axis. This transport results in marine-derived OC dominating southern regions, while terrestrial OC accumulates in the north, accompanied by a corresponding south-to-north decline in organic matter content. Lithology exerts a fundamental control on OC distribution: silty sediments, indicative of turbidity current deposits, display higher TOC and lower SSA, whereas sandy, volcanogenic deposits exhibit elevated SSA and reduced OC loading. Seismic and volcanic disturbances significantly enhance sediment heterogeneity, homogenize oxygen penetration depths and mineralization profiles perpendicular to the axis, and accelerate OC burial by transporting material from both the landward slope and abyssal plain towards the trench axis. This process intensifies mineralization within the axial zone, manifesting as pronounced nitrification in disturbed profiles. Critically, rapid surface mineralization protects deeper OC pools, while volcanic ash dilutes labile organic matter and suppresses microbial activity, thus enhancing long-term carbon sequestration. The dominance of episodic events is underscored by earthquake-triggered turbidity currents, which deposit sediment at rates 20-fold higher than steady-state sedimentation, thereby transporting and preserving organic matter far more effectively. Collectively, these findings provide evidence challenging the steady-state sedimentation paradigm for hadal carbon cycling. We demonstrate that eventdriven deposition—powered by frequent seismic and volcanic activity—constitutes a major, previously underestimated pathway for OC input and burial, likely dominating carbon cycling within the Kermadec Trench and potentially applicable to active subduction zones globally. Future research should therefore prioritize quantifying the global flux of carbon burial via these event-driven processes, integrating high-resolution monitoring of turbidity currents and volcanic inputs with long-term

biogeochemical models. Comparative studies across trenches with varying tectonic activity, sediment supply, and volcanic inputs are also essential to constrain the universality of this mechanism and its contribution to the oceanic carbon budget.

## Data availability statement

The raw data supporting the conclusions of this article will be made available by the authors, without undue reservation.

### **Author contributions**

ZW: Conceptualization, Funding acquisition, Investigation, Methodology, Supervision, Writing – review & editing. SB: Data curation, Investigation, Methodology, Writing – original draft. HX: Investigation, Methodology, Writing – original draft. LD: Investigation, Methodology, Writing – review & editing.

## **Funding**

The author(s) declare financial support was received for the research and/or publication of this article. This work was funded by the National Key Research and Development Program of China (grant nos. 2022YFC2805400) and the National Natural Science Foundation of China (grant nos. 42276059 and 42576036).

## Acknowledgments

We extend sincere gratitude to all members of the 2022 China-New Zealand Joint Hadal Expedition (TS29 Cruise), led by Chief Scientist Prof. Peng Xiaotong, for their collaborative efforts in field sampling and scientific operations. Special appreciation is owed to the crew of the R/V Exploration-1 and the pilots of the Fendouzhe submersible for enabling the successful execution of deep-sea investigations in the Kermadec Trench.

### Conflict of interest

The authors declare that the research was conducted in the absence of any commercial or financial relationships that could be construed as a potential conflict of interest.

### Generative AI statement

The author(s) declare that no Generative AI was used in the creation of this manuscript.

Any alternative text (alt text) provided alongside figures in this article has been generated by Frontiers with the support of artificial intelligence and reasonable efforts have been made to ensure accuracy, including review by the authors wherever possible. If you identify any issues, please contact us.

### Publisher's note

All claims expressed in this article are solely those of the authors and do not necessarily represent those of their affiliated organizations, or those of the publisher, the editors and the reviewers. Any product that may be evaluated in this article, or claim that may be made by its manufacturer, is not guaranteed or endorsed by the publisher.

# Supplementary material

The Supplementary Material for this article can be found online at: https://www.frontiersin.org/articles/10.3389/fmars.2025.1661587/full#supplementary-material

## References

Adamo, P., Marchettiello, A., and Violante, P. (1993). The weathering of mafic rocks by lichens. *Lichenol.* 25, 285–297. doi: 10.1006/lich.1993.1033

Andersson, A. (2011). A systematic examination of a random sampling strategy for source apportionment calculations. *Sci. Total Environ.* 412, 232–238. doi: 10.1016/j.scitotenv.2011.10.031

Argentino, C., Kalenitchenko, D., Lindgren, M., and Panieri, G. (2023).  $HgCl_2$  addition to pore water samples from cold seeps can affect the geochemistry of dissolved inorganic carbon (DIC,  $\delta^{13}$ CDIC). *Mar. Chem.* 251, 104236. doi: 10.1016/j.marchem.2023.104236

Arndt, S., Jorgensen, B., LaRowe, D., Middelburg, J., Pancost, R., and Regnier, P. (2013). Quantifying the degradation of organic matter in marine sediments: A review and synthesis. *Earth-Sci. Rev.* 123, 53–86. doi: 10.1016/j.earscirev.2013.02.008

Arnosti, C., Wietz, M., Brinkhoff, T., Hehemann, J., Probandt, D., Zeugner, L., et al. (2021). The biogeochemistry of marine polysaccharides: Sources, inventories, and bacterial drivers of the carbohydrate cycle. *Annu. Rev. Mar. Sci.* 13, 81–108. doi: 10.1146/annurev-marine-032020-012810

Behrenfeld, M., and Falkowski, P. (1997). Photosynthetic rates derived from satellite-based chlorophyll concentration. *Limnol. Oceanogr.* 42, 1–20. doi: 10.4319/lo.1997.42.1.0001

Blair, N., and Aller, R. (2012). The fate of terrestrial organic carbon in the marine environment. *Annu. Rev. Mar. Sci.* 4, 401–423. doi: 10.1146/annurev-marine-120709-142717

Cai, R., and Jiao, N. (2023). Recalcitrant dissolved organic matter and its major production and removal processes in the ocean. *Deep-Sea Res. I* 191, 10392. doi: 10.1016/j.dsr.2022.103922

Cai, W., Luther, G., Cornwell, J., and Giblin, A. (2010). Carbon cycling and the coupling between proton and electron transfer reactions in aquatic sediments in Lake Champlain. *Aquat. Geochem.* 16, 421–446. doi: 10.1007/s10498-010-9097-9

Chen, S., Meng, Y., Lin, S., Yu, Y., and Xi, J. (2023). Estimation of sea surface nitrate from space: Current status and future potential. *Sci. Total Environ.* 899, 165690. doi: 10.1016/j.scitotenv.2023.165690

Du, M., Peng, X., Zhang, H., Ye, C., Dasgupta, S., Li, J., et al. (2021). Geology, environment, and life in the deepest part of the world's oceans. *Innovation* 2, 100109. doi: 10.1016/j.xinn.2021.100109

Fang, J., Barcelona, M., Nogi, Y., and Kato, C. (2000). Biochemical implications and geochemical significance of novel phospholipids of the extremely barophilic bacteria

from the Marianas Trench at 11,000 m. Deep-Sea Res. I 47, 1173-1182. doi: 10.1016/s0967-0637(99)00080-1

Fernandes, S., Javanaud, C., Michotey, V., Guasco, S., Anschutz, P., and Bonin, P. (2016). Coupling of bacterial nitrification with denitrification and anammox supports N removal in intertidal sediments (Arcachon Bay, France). *Estuar. Coast. Shelf Sci.* 179, 39–50. doi: 10.1016/j.ecss.2015.10.009

George, R., Turner, S., Morris, J., Plank, T., Hawkesworth, C., and Ryan, J. (2005). Pressure-temperature-time paths of sediment recycling beneath the Tonga-Kermadec arc. *Earth Planet. Sci. Lett.* 233, 195–211. doi: 10.1016/j.epsl.2005.01.020

Germineaud, C., Cravatte, S., Sprintall, J., Alberty, M., Grenier, M., and Ganachaud, A. (2021). Deep pacific circulation: New insights on pathways through the Solomon Sea. *Deep-Sea Res. I* 171, 103510. doi: 10.1016/j.dsr.2021.103510

Glud, R. (2008). Oxygen dynamics of marine sediments. *Mar. Biol. Res.* 4, 243–289. doi: 10.1080/17451000801888726

Glud, R. N., Wenzhoefer, F., Middelboe, M., Oguri, K., Turnewitsch, R., and Canfield, D. E. (2013). High rates of microbial carbon turnover in sediments in the deepest oceanic trench on Earth. *Nat. Geosci.* 6, 284–288. doi: 10.1038/NGEO1773

Hoffmann, L. J., Breitbarth, E., Ardelan, M. V., Duggen, S., Olgun, N., Hassellov, M., et al. (2012). Influence of trace metal release from volcanic ash on growth of *Thalassiosira pseudonana* and *Emiliania huxleyi*. *Mar. Chem.* 132, 28–33. doi: 10.1016/j.marchem.2012.02.003

Huang, W., Guo, X., Zhao, J., Li, D., Hu, J., Zhang, H., et al. (2023). Low content of highly reactive iron in sediments from Prydz Bay and the adjacent Southern Ocean: Controlling factors and implications for sedimentary organic carbon preservation. *Front. Mar. Sci.* 10. doi: 10.3389/fmars.2023.1142061

Jamieson, A. J., Stewart, H. A., Rowden, A. A., and Clark, M. R. (2020). "Chapter 59 - Geomorphology and benthic habitats of the Kermadec Trench, southwest Pacific Ocean," in *Seafloor Geomorphology as Benthic Habitat, 2nd ed.* Eds. P. T. Harris and E. Baker (Elsevier), 949–966.

Jiao, N. Z. (2012). Carbon fixation and sequestration in the ocean, with special reference to the microbial carbon pump. *Sci. Sin. Terrae* 42, 1473–1486. doi: CNKI: SUN:IDXK.0.2012-10-003

Kioka, A., Schwestermann, T., Moernaut, J., Ikehara, K., Kanamatsu, T., McHugh, C. M., et al. (2019). Megathrust earthquake drives drastic organic carbon supply to the hadal trench. *Sci. Rep.* 9, 1553. doi: 10.1038/s41598-019-38834-x

Krause-Jensen, D., and Duarte, C. (2016). Substantial role of macroalgae in marine carbon sequestration. *Nat. Geosci.* 9, 737. doi: 10.1038/ngeo2790

Leithold, E., Blair, N., and Perkey, D. (2006). Geomorphologic controls on the age of particulate organic carbon from small mountainous and upland rivers. *Global Biogeochem. Cycles* 20, GB3022. doi: 10.1029/2005gb002677

Lemenkova, P. (2019). GMT based comparative analysis and geomorphological mapping of the Kermadec and Tonga trenches, southwest pacific ocean. *Geographia Technica*. 14, 39–48 doi: 10.21163/GT\_2019.142.04

Leslie, H., Brandsma, S., van Velzen, M., and Vethaak, A. (2017). Microplastics en route: Field measurements in the Dutch river delta and Amsterdam canals, wastewater treatment plants, North Sea sediments and biota. *Environ. Int.* 101, 133–142. doi: 10.1016/j.envint.2017.01.018

Li, Z., Wang, X., Jin, H., Ji, Z., Bai, Y., and Chen, J. (2017). Variations in organic carbon loading of surface sediments from the shelf to the slope of the Chukchi Sea, Arctic Ocean. *Acta Oceanol. Sin.* 36, 131–136. doi: 10.1007/s13131-017-1026-y

Li, D., Zhao, J., Yao, P., Liu, C., Sun, C., Chen, J., et al. (2020). Spatial heterogeneity of organic carbon cycling in sediments of the northern Yap Trench: Implications for organic carbon burial. *Mar. Chem.* 223, 103813. doi: 10.1016/j.marchem.2020.103813

Lin, B., Liu, Z., Eglinton, T. I., Wiesner, M. G., Blattmann, T. M., and Haghipour, N. (2024). Organic carbon sources in surface sediments on the northern South China Sea. *J. Geophys. Res. Biogeosci.* 129, e2023JG007909. doi: 10.1029/2023jg007909

Linley, T. D., Stewart, A. L., McMillan, P. J., Clark, M. R., Gerringer, M. E., Drazen, J. C., et al. (2017). Bait attending fishes of the abyssal zone and hadal boundary: Community structure, functional groups and species distribution in the Kermadec, New Hebrides and Mariana trenches. *Deep-Sea Res. I* 121, 38–53. doi: 10.1016/j.dsr.2016.12.009

Liu, S., Peng, X., Yang, H., Zhang, X., Qu, Y., Li, J., et al. (2023). A novel iron biomineralization on basaltic rocks from the Challenger Deep, southern Mariana Trench. *Chem. Geol.* 635, 121617. doi: 10.1016/j.chemgeo.2023.121617

Longman, J., Palmer, M., Gernon, T., and Manners, H. (2019). The role of tephra in enhancing organic carbon preservation in marine sediments. *Earth-Sci. Rev.* 192, 480–490. doi: 10.1016/j.earscirev.2019.03.018

Luo, M., Gieskes, J., Chen, L., Scholten, J., Pan, B., Lin, G., et al. (2019). Sources, degradation, and transport of organic matter in the New Britain Shelf-Trench Continuum, Papua New Guinea. *J. Geophys. Res. Biogeosci.* 124, 1680–1695. doi: 10.1029/2018jg004691

Luo, M., Glud, R., Pan, B., Wenzhöfer, F., Xu, Y., Lin, G., et al. (2018). Benthic carbon mineralization in hadal trenches: Insights From in *situ* determination of benthic oxygen consumption. *Geophys. Res. Lett.* 45, 2752–2760. doi: 10.1002/2017gl076232

Luo, M., Zheng, M., Wallmann, K., Dale, A., Strasser, M., Torres, M., et al. (2025). Rapid burial and intense degradation of organic matter drive active silicate weathering in the subsurface sediments of the ocean's deepest realm. *Geology*. 53 (8), 636–641. doi: 10.1130/g53131.1

Marsay, C., Sanders, R., Henson, S., Pabortsava, K., Achterberg, E., and Lampitt, R. (2015). Attenuation of sinking particulate organic carbon flux through the mesopelagic ocean. *Proc. Natl. Acad. Sci. U.S.A.* 112, 1089–1094. doi: 10.1073/pnas.1415311112

Mayer, L. (1994). The surface-area control of organic-carbon accumulation in continental-shelf sediments. *Geochim. Cosmochim. Acta* 58, 1271–1284. doi: 10.1016/0016-7037(94)90381-6

Oguri, K., Kawamura, K., Sakaguchi, A., Toyofuku, T., Kasaya, T., Murayama, M., et al. (2013). Hadal disturbance in the Japan Trench induced by the 2011 Tohoku-Oki Earthquake. *Sci. Rep.* 3, 1915. doi: 10.1038/srep01915

Oguri, K., Masqué, P., Zabel, M., Stewart, H., MacKinnon, G., Rowden, A., et al. (2022). Sediment accumulation and carbon burial in four hadal trench systems. *J. Geophys. Res. Biogeosci.* 127, e2022JG006814. doi: 10.1029/2022jg006814

Peng, X., Zhang, W., Schnabel, K., Leduc, D., Xu, H., Zhang, H., et al. (2023). Unveiling the mysteries of the kermadec trench. *Innovation* 4, 100367. doi: 10.1016/j.xinn.2022.100367

Peoples, L., Donaldson, S., Osuntokun, O., Xia, Q., Nelson, A., Blanton, J., et al. (2018). Vertically distinct microbial communities in the Mariana and Kermadec trenches. *PloS One* 13 (4), e0195102. doi: 10.1371/journal.pone.0195102

Peoples, L., Grammatopoulou, E., Pombrol, M., Xu, X., Osuntokun, O., Blanton, J., et al. (2019). Microbial community diversity within sediments from two geographically separated hadal trenches. *Front. Microbiol.* 10. doi: 10.3389/fmicb.2019.00347

Popp, B., Trull, T., Kenig, F., Wakeham, S., Rust, T., Tilbrook, B., et al. (1999). Controls on the carbon isotopic composition of Southern Ocean phytoplankton. *Global Biogeochem. Cycles* 13, 827–843. doi: 10.1029/1999gb900041

Schauberger, C., Glud, R., Hausmann, B., Trouche, B., Maignien, L., Poulain, J., et al. (2021). Microbial community structure in hadal sediments: high similarity along trench axes and strong changes along redox gradients. *ISME J.* 15, 3455–3467. doi: 10.1038/s41396-021-01021-w

Steinberg, D., and Landry, M. (2017). Zooplankton and the ocean carbon cycle. *Annu. Rev. Mar. Sci.* 9, 413–444. doi: 10.1146/annurev-marine-010814-015924

Stewart, H., and Jamieson, A. (2018). Habitat heterogeneity of hadal trenches: Considerations and implications for future studies. *Prog. Oceanogr.* 161, 47–65. doi: 10.1016/j.pocean.2018.01.007

Sudek, L., Wanger, G., Templeton, A., Staudigel, H., and Tebo, B. (2017). Submarine basaltic glass colonization by the heterotrophic fe(II)-oxidizing and siderophore-producing deep-sea bacterium *pseudomonas stutzeri* VS-10: the potential role of basalt in enhancing growth. *Front. Microbiol.* 8. doi: 10.3389/fmicb.2017.00363

Tagliabue, A., Bowie, A., Boyd, P., Buck, K., Johnson, K., and Saito, M. (2017). The integral role of iron in ocean biogeochemistry. *Nat.* 543, 51–59. doi: 10.1038/nature21058

Talling, P., Hage, S., Baker, M., Bianchi, T., Hilton, R., and Maier, K. (2024). The global turbidity current pump and its implications for organic carbon cycling. *Annu. Rev. Mar. Sci.* 16, 105–133. doi: 10.1146/annurev-marine-032223-103626

Turnewitsch, R., Falahat, S., Stehlikova, J., Oguri, K., Glud, R., Middelboe, M., et al. (2014). Recent sediment dynamics in hadal trenches: Evidence for the influence of higher-frequency (tidal, near-inertial) fluid dynamics. *Deep-Sea Res. I* 90, 125–138. doi: 10.1016/j.dsr.2014.05.005

Uroz, S., Calvaruso, C., Turpault, M., and Frey-Klett, P. (2009). Mineral weathering by bacteria: ecology, actors and mechanisms. *Trends Microbiol.* 17, 378–387. doi: 10.1016/j.tim.2009.05.004

Watson, A. (1997). Volcanic iron,  $CO_2$ , ocean productivity and climate. Nat. 385, 587–588. doi: 10.1038/385587b0

Wenzhöfer, F., Oguri, K., Middelboe, M., Turnewitsch, R., Toyofuku, T., Kitazato, H., et al. (2016). Benthic carbon mineralization in hadal trenches: Assessment by in situ O<sub>2</sub> microprofile measurements. *Deep-Sea Res. I* 116, 276–286. doi: 10.1016/i.dsr.2016.08.013

Xiao, W., Xu, Y., Canfield, D., Wenzhöfer, F., Zhang, C., and Glud, R. (2024). Strong linkage between benthic oxygen uptake and bacterial tetraether lipids in deep-sea trench regions. *Nat. Commun.* 15, 3439. doi: 10.1038/s41467-024-47660-3

Xie, J., Zhang, G., Chen, C., Luo, M., Xu, H., Chen, D., et al. (2024). Tracing organophosphate ester pollutants in hadal trenches-distribution, possible origins, and transport mechanisms. *Environ. Sci. Technol.* 58, 4392–4403. doi: 10.1021/acs.est.3ci09884

Xu, Y., Li, X., Luo, M., Xiao, W., Fang, J., Rashid, H., et al. (2021). Distribution, source, and burial of sedimentary organic carbon in Kermadec and Atacama trenches. *J. Geophys. Res. Biogeosci.* 126, e2020JG006189. doi: 10.1029/2020jg006189

Yao, P., Zhao, B., Bianchi, T., Guo, Z., Zhao, M., Li, D., et al. (2014). Remineralization of sedimentary organic carbon in mud deposits of the Changjiang Estuary and adjacent shelf: Implications for carbon preservation and authigenic mineral formation. *Cont. Shelf Res.* 91, 1–11. doi: 10.1016/j.csr.2014.08.010

Ye, L., Hu, Y., Xia, T., Lay, T., Sang, Y., Chen, X., et al. (2025). The 2021 MW 8.1 Kermadec earthquake sequence: Great earthquake rupture along the mantle/slab contact. *J. Geophys. Res. Solid Earth* 130, e2024JB030926. doi: 10.1029/2024jb030926

Zhao, Y., Jia, J., Liu, C., and Feng, X. (2024). Carbon preservation in sedimentary deposits: Beyond mineral protection. *Innovation* 5 (2), 100576. doi: 10.1016/j.xinn.2024.100576